Journal of Materials Chemistry A

ROYAL SOCIETY OF CHEMISTRY

PAPER

View Article Online
View Journal | View Issue

Cite this: J. Mater. Chem. A, 2024, 12, 14816

Origin of sputter damage during transparent conductive oxide deposition for semitransparent perovskite solar cells†

Qing Yang, [ac] Weiyuan Duan, *[a] Alexander Eberst,[ac] Benjamin Klingebiel,[a] Yueming Wang,[ad] Ashish Kulkarni,[ae] Andreas Lambertz,[a] Karsten Bittkau, [a] Yongqiang Zhang,[b] Svetlana Vitusevich, [b] Uwe Rau,*[ac] Thomas Kirchartz [ad] and Kaining Ding*[ac]

Transparent conductive oxides (TCOs) have been widely used as transparent electrodes in numerous optoelectronic devices including perovskite/silicon tandem solar cells. A significant concern regarding the application of TCOs is the sputter-induced damage to the underlying films. Understanding the source of this damage and finding ways to mitigate it are crucial to improve the design of solar cells. In this study, a systematic investigation was performed to determine the origin of TCO sputtering damage on the perovskite/C_{60} stack using various optical filters and a series of sample structures. Our results revealed that the steady-state photoluminescence intensity increased when the perovskite/C_{60} stack was only exposed to plasma radiation. This finding suggests that sputtering damage originates from ion bombardment rather than plasma radiation. X-ray diffraction analysis indicated that the plasma radiation involved in the sputtering process could release the lattice strain in the perovskite film. Furthermore, both simulations and experiments illustrated that sputtering damage was associated with the formation of defects in the C_{60} layer and the dissociation of C=N bonds at the perovskite surface due to ion-bombardment-induced phonon propagation. A method to mitigate this damage using a SnO_x buffer layer was experimentally confirmed, and its working mechanism was elucidated.

Received 31st October 2023
Accepted 11th April 2024

DOI: 10.1039/d3ta06654a

rsc.li/materials-a

1. Introduction

In recent years, halide perovskites have garnered significant attention owing to their tunable bandgaps,[1] high absorption coefficients,[2] long charge-carrier lifetimes[3] and simple fabrication methods.[4–8] The efficiency of single-junction perovskite solar cells (PSCs) has witnessed remarkable growth, overcoming 26% within just a decade.[9] Although crystalline silicon solar cells currently dominate over 90% of the photovoltaic (PV) market,[10] their efficiency is approaching the practical limit defined by Auger recombination, thermalization, and transmission losses.[11] To further improve the conversion efficiency of solar cells, tandem structures have emerged as a promising solution.[12] These structures involve adding a higher bandgap absorber on top of silicon solar cells, enabling better utilization of the solar spectrum and reducing thermalization loss.[11] Among the existing tandem combinations, monolithic perovskite/silicon solar cells are the most promising candidates, with their highest efficiency rapidly increasing from 13.7% (ref. 13) to 33.9% (ref. 14) over the last few years.

In single-junction PSCs, all layers are fabricated sequentially from bottom to top on a glass substrate with a tin-doped indium oxide (ITO) coating and finished with an opaque electrode; thus, the cell performance can only be measured from the glass side. When PSCs with an inverted structure (p-i-n) are applied as the top cells in perovskite/silicon tandem solar cells, the hole-transporting layer (HTL), perovskite layer, electron-transporting layer (ETL), and electrode are fabricated sequentially on the silicon bottom cells. The opaque electrode was replaced with transparent conductive oxides (TCOs) to allow illumination to enter the cell from the ETL side. In general, TCOs are mostly prepared by sputtering, which offers advantages such as high deposition rates, excellent adhesion, and uniformity.[15–18] However, the sputtering process of TCOs tends to damage the underlying organic layers, particularly the

[a]IEK-5 Photovoltaics, Forschungszentrum Jülich GmbH, Wilhelm-Johnen Straße, 52425 Jülich, Germany. E-mail: w.duan@fz-juelich.de; u.rau@fz-juelich.de; k.ding@fz-juelich.de

[b]IBI-3 Institute of Biological Information Processing, Forschungszentrum Jülich GmbH, Wilhelm-Johnen Straße, 52425 Jülich, Germany

[c]Faculty of Electrical Engineering and Information Technology, RWTH Aachen University, 7 Mies-van-der-Rohe-Straße 15, 52074 Aachen, Germany

[d]Faculty of Engineering and CENIDE, University of Duisburg-Essen, Carl-Benz-Str. 199, 47057 Duisburg, Germany

[e]Institute of Inorganic Chemistry, University of Cologne, Greinstr. 6, 50939 Cologne, Germany

† Electronic supplementary information (ESI) available. See DOI: https://doi.org/10.1039/d3ta06654a

perovskite layer.[19,20] Zanoni *et al.* reported that the accelerated particles, together with side effects such as plasma radiation and process-induced heat, can easily damage soft organic semiconductor layers, resulting in leakage currents, efficiency deterioration and lifetime degradation.[21] Mariotti *et al.* have revealed that the plasma UV radiation during sputtering has a negative impact on the path length of particles and the kinetic energy of hitting substrate.[22] Regarding the concern of performance deterioration, various strategies have been proposed to minimize the sputtering damage, such as inserting buffer layer,[23,24] using a soft sputtering deposition by lowering sputter power density,[25] or adopting pulsed laser deposition as an alternative technique.[26,27] Although a soft sputtering process holds promise for minimizing sputtering damage, our investigation on the optoelectrical properties of ITO revealed that decreasing the sputtering power from 50 W to 30 W led to a dramatic increase in the sheet resistance from 40 Ω sq^{-1} to 2000 Ω sq^{-1}, resulting in a significant series resistance loss and ultimately deteriorating device performance. Therefore, a holistic evaluation, balancing considerations of sputtering damage with the intricate balance of optical and electrical properties of TCOs, is necessary, especially for their application in perovskite/silicon tandem solar cells. Use of a SnO_x buffer layer is a typical well-known approach to avoid sputtering damage.[12]

The conventional understanding of the origin of sputtering damage is attributed to high-kinetic-energy ion bombardment and/or plasma radiation generated during the sputtering process.[21–23] However, two critical issues have been overlooked. First, prior investigations did not address the structural alterations in sputtering-prone layers, including defects, lattice strain, and chemical bonds within films or on their surfaces.[20,25,28] Second, although considerable attention has been directed towards the combined effects of ion bombardment and plasma radiation, the distinct influence of each factor on films, stacks, and devices remains largely unexplored. To address this gap, we utilized various optical filters to decouple ion bombardment and plasma radiation, allowing us to investigate their individual impacts on bare films, layer stacks, and complete devices. Our methodology aims to shed light on the factors causing sputtering damage in perovskite-related devices and the resulting structural changes in the susceptible layers. Ultimately, this research will help us understand the mechanisms underlying performance deterioration during TCO sputtering. Furthermore, this work can guide the optimization of the sputtering process and the selection of appropriate buffer layers prior to the fabrication of transparent electrodes.

In this study, steady-state photoluminescence (ssPL) spectra of perovskite/C_{60} samples were investigated, and various optical filters were applied during ITO sputtering. The aim was to distinguish between the effects of plasma radiation and high-kinetic-energy ion bombardment during sputtering. In addition, a simulation analysis of the penetration depth profile of the incident ions in the perovskite/C_{60} stack was performed using the Stopping and Range of Ions in the Matter (SRIM) software. The purpose of this analysis was to determine whether the incident ions directly damaged the perovskite layer. Moreover, the energy-loss distribution of the incident ions was calculated to gain insight into the energy transferred to the perovskite/C_{60} films. Finally, an efficient semi-transparent perovskite solar cell was successfully fabricated by implementing an SnO_x buffer layer to effectively protect the perovskite/C_{60} stack.

2. Results and discussion

First, we studied the source of the sputtering damage during ITO deposition through two experiments: (1) covering the samples using an optical filter with a specific cutoff wavelength in transmittance, and (2) exposing the samples directly to the plasma. Sketches of the samples are shown in Fig. 1a. An optical filter is the key tool for decoupling plasma radiation and ion bombardment, allowing us to investigate their individual impacts and shed light on the factors causing sputtering

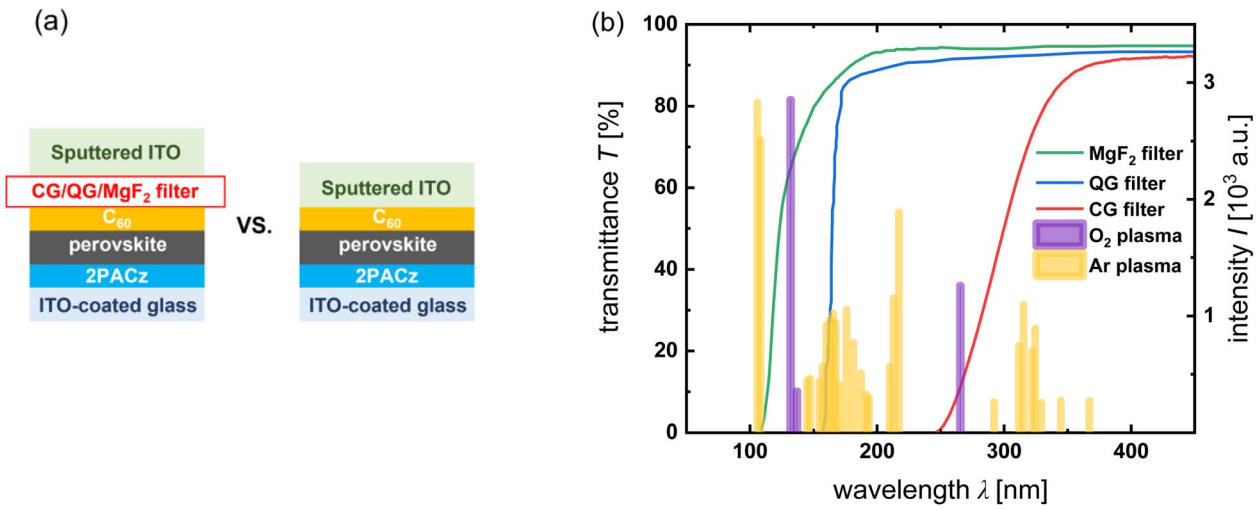

Fig. 1 (a) Sketches of the samples for PL measurement with and without optical filters. (b) Transmittance spectra of three filters and the optical emission spectrum of oxygen/argon plasma.[29]

damage; however, it cannot be used as a buffer layer to mitigate the damage. During the ITO sputtering process, the shielded samples were only accessible to oxygen/argon plasma radiation, because the filters blocked the bombardment of ions and other particles. In contrast, the samples that were not covered with a filter were exposed to the entire sputtering process, including plasma radiation and high-kinetic-energy ion bombardment. Three optical filters were utilized: corning glass (CG), quartz glass (QG), and magnesium fluoride-coated glass (MgF_2). The transmittance curves of these filters and the optical emission spectra of the oxygen and argon plasma generated during sputtering are shown in Fig. 1b. The CG filter allows photon transmission with wavelengths above 250 nm, which enables approximately 10% transmittance at the emission peak of 265.5 nm related to the oxygen plasma and up to 90% transmittance at emission peaks ranging from 290 to 370 nm associated with the argon plasma. The QG filter has a cutoff wavelength of 160 nm, enabling up to 90% transmittance of argon plasma at shorter emission wavelengths. The MgF_2 filter extends the minimum transmission wavelength to 110 nm, which is transparent to strong oxygen plasma at approximately 131 nm.

PL spectroscopy is a suitable tool for studying the effects of process variations on the nonradiative recombination in semiconductors. The higher the PL intensity at a given excitation, the higher the fraction of radiative recombination and the lower the fraction of unwanted nonradiative recombination. As process variations typically primarily affect nonradiative recombination, comparing absolute or relative PL intensities as a function of sample geometry or processing is a simple but effective strategy for evaluating changes in recombination without requiring electrical contacts. Thus, we studied the absolute PL spectra and quantum yields of the covered and uncovered samples using a PL setup from QY Berlin. Therefore, we distinguished between the effects of plasma radiation and ion bombardment on the glass/ITO/2PACz/perovskite/C_{60} stack during ITO sputtering, where 2PACz and C_{60} acted as HTL and ETL, respectively. The exposure time to plasma radiation was 35 min, which was also the deposition time, implying that a 110 nm ITO film was deposited on top of either the filter or C_{60} at the end of the experiments. Notably, the transparency of the highly transparent ITO increased as the layer thickness decreased, indicating a potential shift towards the optical filter with increased thickness as the exposure time increased, although this outcome was inevitable. The transmittance curves of both the 10 nm and 110 nm ITO films deposited on the CG filter are given in the ESI (Fig. S9†) for reference. In the early stage of sputtering, the thin ITO film exhibited almost complete transparency to plasma radiation. However, it has become challenging to accurately assess the impact of the exposure time to plasma radiation on PL and determine the optimal exposure time because of the inherent filtering effect of thick ITO.

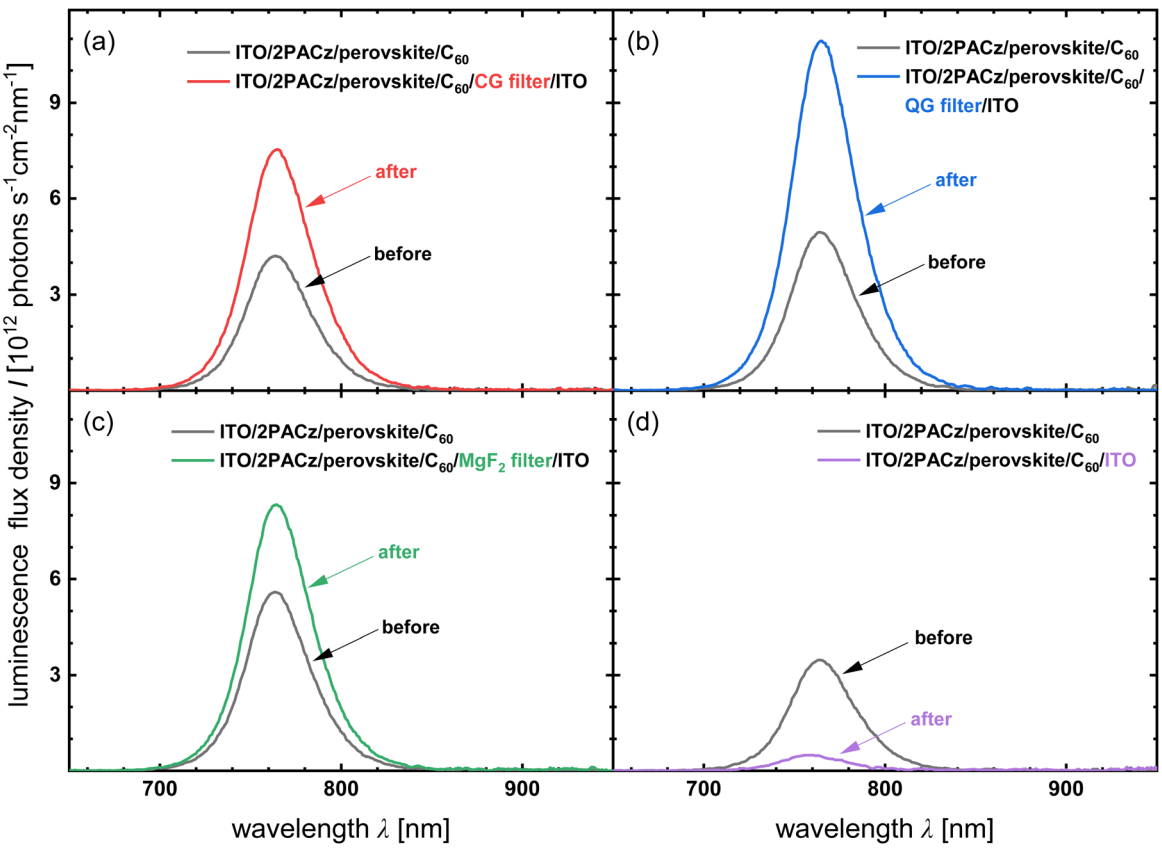

Fig. 2 PL spectra of stacks shielded by (a) corning glass (CG), (b) quartz glass (QG), (c) magnesium fluoride-coated glass (MgF_2), and (d) without filter before and after ITO sputtering.

Although pure plasma treatment without sputtering is an alternative method, it fails to replicate authentic experimental conditions effectively.

In Fig. 2a–c, it is evident that the PL intensities of the layer stacks shielded by the optical filters exhibit an enhancement under different plasma radiation conditions. However, the PL intensity decreased significantly when ITO was directly sputtered onto the C_{60} film, as shown in Fig. 2d. The full width at half maximum (FWHM) values before and after ITO sputtering in the four scenarios are listed in Table 1, with negligible changes (see ESI†). The statistics of the PL intensity in the four scenarios demonstrated the good reproducibility of the intensity variation (Fig. S1†). The results reveal that sputtering damage to the underlying stack primarily arises from ion bombardment, and the resulting degradation far outweighs any gain from plasma radiation. To examine the positive effect of plasma radiation, the rate of change in the luminescence flux density was plotted against the implied open-circuit voltage (iV_{OC}) of each sample before and after ITO sputtering (Fig. S1†). iV_{OC} increased as the PL intensity increased when the ions were completely blocked by the filters. This observation suggests that the oxygen/argon plasma radiation effectively suppressed the nonradiative recombination in the glass/ITO/2PACz/perovskite/C_{60} stacks. Given that previous reports have found correlations between lattice strain and nonradiative recombination,[30–32] further investigations were carried out to study the change in lattice strain within perovskite films. The findings are discussed in the next section.

X-ray diffraction (XRD) was carried out to study the variation in the crystal structure and lattice strain in the perovskite films after ITO sputtering under the above two conditions. Before the XRD measurements, the C_{60} and top sputtered ITO layers on the "plasma radiation & ion bombardment" sample were washed away by dynamically spin-coating chlorobenzene (CB) solution. The CB solution dissolved C_{60} but did not affect the perovskite layer (Fig. S1†). In Fig. 3a, diffraction peaks corresponding to the various crystal planes of the perovskite are observed in the specially treated perovskite films (red and blue lines) and the perovskite control sample (purple line). The XRD patterns of all samples contain the same typical perovskite peak at ~14°, corresponding to the (100) crystallographic plane. This observation indicates that ITO sputtering did not change the crystal

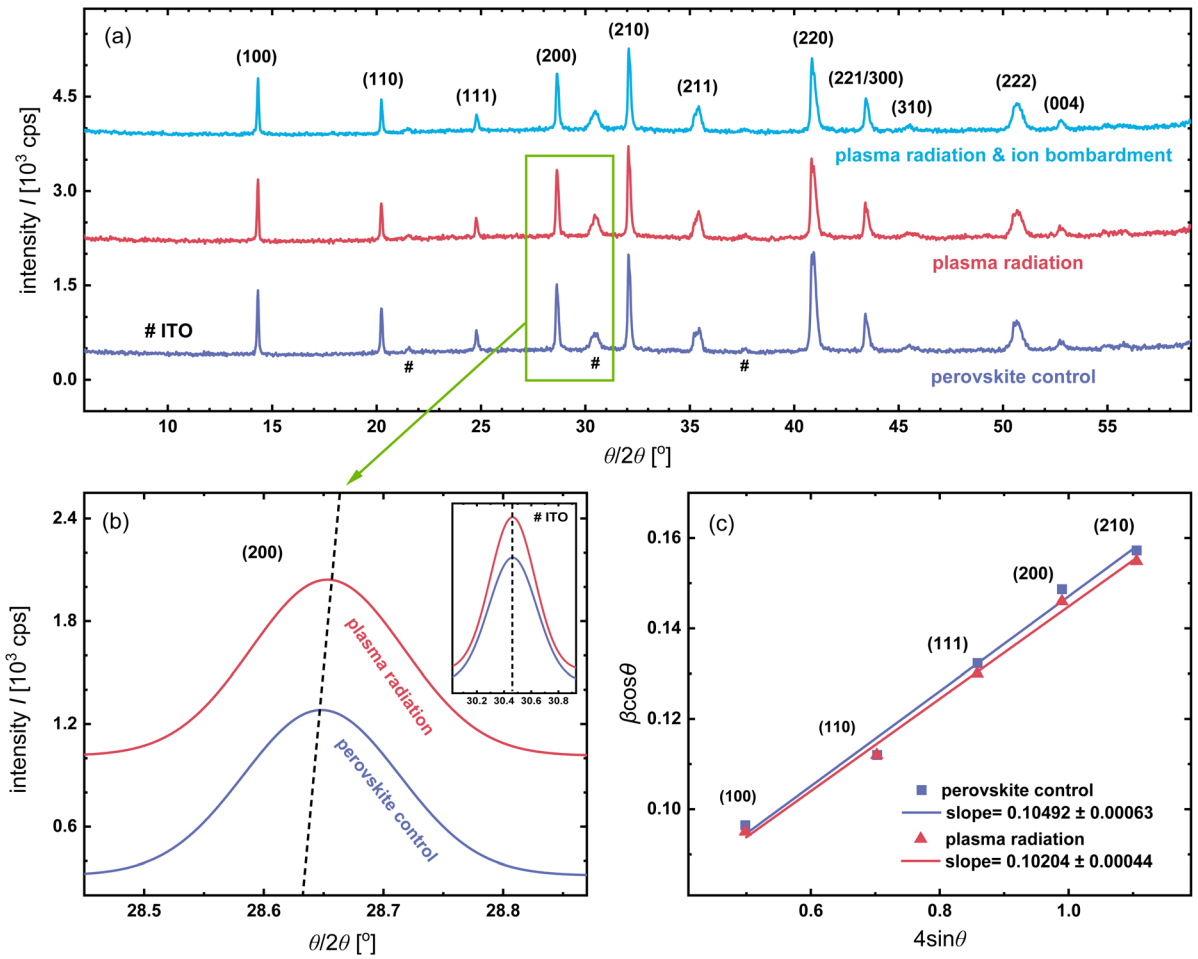

Fig. 3 (a) XRD patterns of the control perovskite film, perovskite film covered using an optical filter, and perovskite film exposed directly to plasma. (b) Magnified (200) plane diffraction peaks and ITO characteristic peaks. (c) Williamson–Hall plots for each sample. The zoomed-in operation of the XRD patterns and the different magnifications of the *x*- and *y*-axes make the shapes of the magnified peaks different from those of the original one.

structure of the perovskite. Furthermore, there is no evidence of phase segregation, as no side peak was found at 11.6°, which is related to the photoinactive hexagonal δ-phase of $FAPbI_3$.[33] The XRD patterns of the samples also included three specific peaks of ITO (labeled #), which originated from the ITO-coated glass. We observed that the diffraction peak of (200) broadened slightly and red-shifted to angles larger than 28.63° after the perovskite/C_{60} stack was treated with plasma radiation, as depicted in Fig. 3b. In addition, the same broadening of other four diffraction peaks was observed after plasma radiation, including (100), (110), (111), and (210), suggesting the presence of lattice strain in perovskite films.[34]

To estimate the lattice strain within the perovskite films, the Williamson–Hall (W–H) method was utilized to analyze the diffraction peak broadening in-depth,[35] which can be attributed to the crystallite-size-induced broadening β_L (1) and strain-induced broadening β_e (2).

$$\beta_L = \frac{K\lambda}{L\cos\theta} \quad (1)$$

where β is the FWHM of the diffraction peak, L is the crystallite size, and λ is the X-ray wavelength. The strain-induced broadening β_e (2) is calculated from

$$\beta_e = C\varepsilon\tan\theta \quad (2)$$

where ε is the strain and C is a constant value (typically ≈ 4). If both contributions are present, then the combined effects should be determined by convolution. A simple sum is assumed to be a convolution for simplification (3).

$$\beta\cos\theta = C\varepsilon\sin\theta + \frac{K\lambda}{L} \quad (3)$$

The size and strain components can be obtained from the intercept ($K\lambda/L$) and slope (ε) by plotting $\beta\cos\theta$ *versus* $4\sin\theta$, respectively. In general, the fabrication process determines the crystallite size of the perovskites.[36] In this study, the contribution of the β_L component could be neglected because the perovskite films were prepared simultaneously using the same spin-coating and post-annealing processes, resulting in the same crystallite size. The W–H plots of the perovskite control and the perovskite film treated with plasma radiation are shown in Fig. 3c, where the broadening diffraction peaks are considered as a function of the diffraction angle. The positive slopes of the fitting curves indicate the presence of lattice expansion in both samples. The slope of the W–H plots of the perovskite film treated with plasma radiation was 0.10204 ± 0.00044, which was smaller than the slope of 0.10492 ± 0.00063 for the perovskite control, suggesting relaxation of the lattice strain. In principle, the release of lattice strain contributes to the yield of higher iV_{OC} due to the reduction in defect concentration and the suppression of nonradiative recombination.[30,32] In the previous analysis of PL spectra, we observed an increase in the iV_{OC} of the glass/ITO/2PACz/perovskite/C_{60} stacks after plasma radiation and inferred that plasma radiation reduced nonradiative recombination within the perovskite films by releasing the lattice strain.[37] It also illustrates that ion bombardment was the dominant cause of sputtering damage in this study, instead of plasma radiation. However, in the absence of a reliable method for decoupling the oxygen and argon plasma, we cannot determine whether oxygen plasma or argon plasma is the primary source of sputtering damage. When examining the reasons behind the relaxation of lattice strains due to plasma radiation, we should recognize that the light-induced alterations in lattice strain depend on various parameters, including photon energy,[38] wavelength,[39] intensity, and duration of illumination.[37,40] Given the potential of each of these factors to impact lattice strain through distinct mechanisms, and considering that plasma radiation was not identified as the primary contributor to sputtering damage, we refrained from conducting a separate and comprehensive study in the present work. Further research and analysis are necessary to compressively address this unresolved aspect.

Single-junction PSCs were fabricated to evaluate the impact of the plasma radiation. Both the control and the "plasma radiation" PSCs have the same architecture given by glass/ITO/2PACz/perovskite/C_{60}/BCP/Ag. The control devices adhere to a standard procedure, while the "plasma radiation" devices undergo a slightly different manufacturing process. In the case of the "plasma radiation" devices, after preparing the glass/ITO/2PACz/perovskite/C_{60} stacks, they were promptly covered with CG filters. Subsequently, they were transferred to a sputtering chamber for post-treatment with plasma radiation during ITO sputtering. Importantly, it should be noted that the CG filters effectively block ions during this process. Following the plasma radiation treatment, the samples were returned to a glovebox for deposition of the BCP/Ag layers. Compared with the control devices, the "plasma radiation" devices exhibit an average efficiency enhancement of more than 1%, as depicted in Fig. 4. The enhanced efficiency (η) of PSCs following exposure to plasma radiation can be attributed to the relaxation of lattice strain. This relaxation effectively suppresses nonradiative recombination within the perovskite films, thereby enabling a more efficient collection of carriers, which results in an increase in the open-circuit voltage (V_{OC}) and fill factor (FF).

From the XRD results, it is difficult to determine whether ion bombardment is damaging to the perovskite film; therefore, more detailed studies of perovskite films have been performed. Two sample configurations were investigated with PL: glass/ITO/2PACz/perovskite/C_{60}/(SnO_x/)ITO stacks with or without SnO_x and glass/ITO/2PACz/perovskite stacks. The latter samples were obtained by washing away the C_{60}/(SnO_x/)ITO films of the former one with CB, as shown in Fig. 5c. The sample employed a commonly used buffer layer, SnO_x, on top of C_{60} to mitigate sputtering damage (see ESI† for more details on SnO_x deposition). As shown in Fig. 5a, there was no degradation in the PL intensity after ITO sputtering in the sample containing SnO_x (solid lines). In contrast, the PL intensity of the sample without SnO_x is notably diminished (dashed lines). However, the results only illustrate the damage to the entire stack without revealing the impact on the perovskite films individually. Therefore, the second configuration, focused solely on the glass/ITO/2PACz/perovskite stack, was studied to exclude any interference from

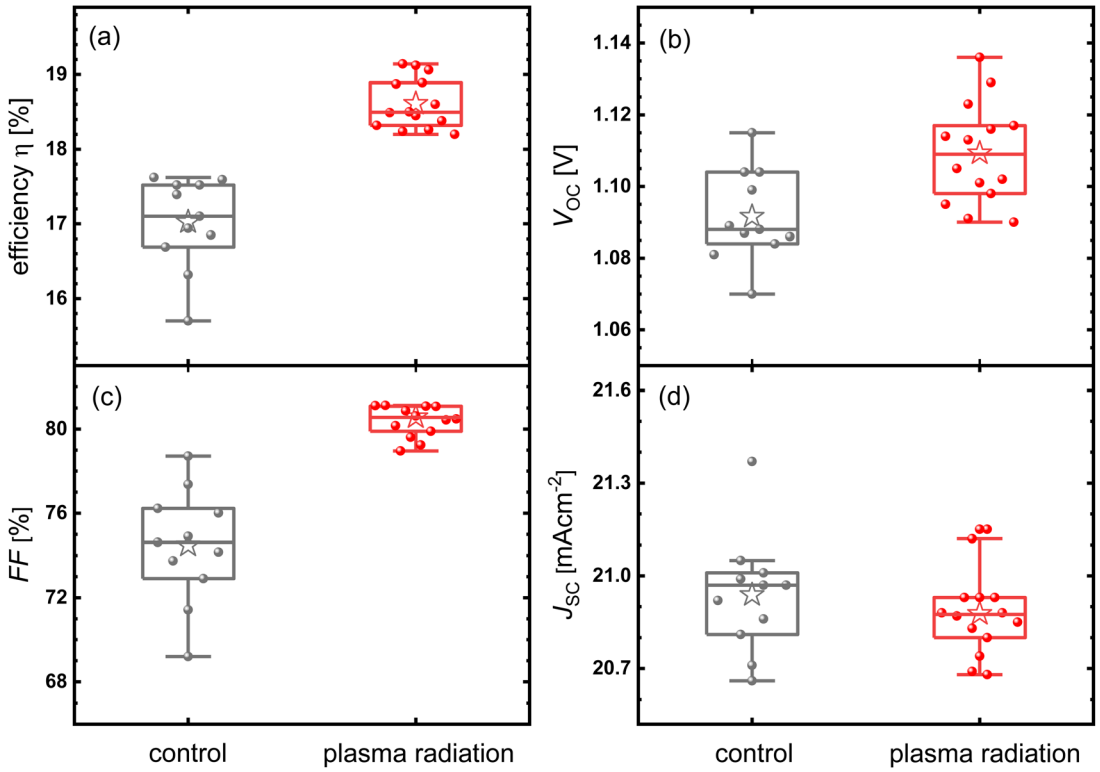

Fig. 4 (a–d) η, V_{OC}, FF, and J_{SC} statistics of the control perovskite solar cells and cells treated with plasma radiation prior to the deposition of the BCP/Ag layers.

other films, particularly C_{60}. After washing away the C_{60}/(SnO_x/)ITO films, their PL spectra were re-measured and compared with that of the control sample, which was an as-prepared glass/ITO/2PACz/perovskite stack, as shown in Fig. 5b. We observed that the PL signals of the sample containing SnO_x and the control sample almost coincided, whereas the PL intensity of

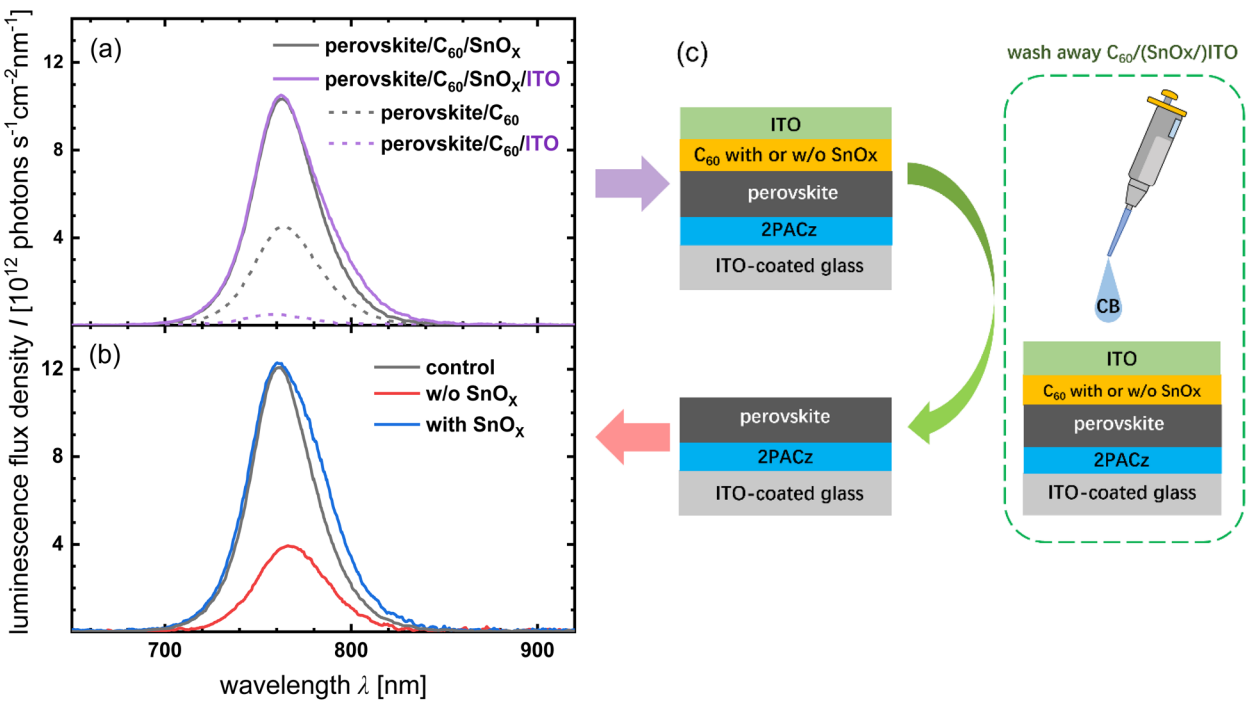

Fig. 5 PL spectra of stacks (a) before and (b) after washing away C_{60}/(SnO_x/)ITO layers. The control sample was the as-prepared perovskite layer on glass/ITO/2PACz/. (c) Schematic of the sample stacks and procedure for film removal.

the sample without SnO_x degraded significantly. This observation demonstrates that the absence of a buffer layer damages the underlying perovskite film after the ITO sputtering. We also observed that the PL intensity of the perovskite/C_{60}/SnO_x sample was higher than that of the perovskite/C_{60} sample, suggesting that the SnO_x treatment enhanced the PL intensity. SnO_x is likely to have a much lower work function than bare C_{60}, which will move the Fermi level at the perovskite/C_{60} interface up towards the conduction band of C_{60}. This will reduce the hole concentration in the perovskite at the interface, thereby reducing the recombination rate at a given Fermi level splitting. This leads to enhanced PL.

To determine whether sputtering damage to the perovskite film is associated with ion penetration, SRIM Monte Carlo simulations were carried out to simulate the penetration depth of the negative ions with an initial kinetic energy of 85 eV, which was calculated from the voltage between the target and substrate during ITO sputtering (see the ESI† for detailed settings). Fig. 6a shows the ion distributions of oxygen, argon, indium, and tin in the perovskite/C_{60} stack as a function of the penetration depth. Oxygen and argon ions have penetration depths of ~3 nm, whereas tin and indium ions have maximum penetration depths of ~4 nm. All impinging ions eventually stopped penetrating to a depth of less than 5 nm from the surface and remained in the C_{60} film. The white and red dots displayed in the black background represent the moving ions and stopped atoms ejected from their original site when collisions transfer more than the displacement energy (E_{disp}). The radial and spherical distributions of the atoms were attributed to the penetration of the heavy and light ions, respectively. For semiconductors, the typical values of E_{disp} are about 15 eV,[41] which is significantly lower than the initial kinetic energy of ions. Subsequently, vacancies were created near the surface owing to the collisions between the ions and lattice atoms as well as the collisions between the recoiling atoms and other lattice atoms. Recoiling atoms, also known as recoils, are atoms that are knocked out of their lattice sites, thus creating vacancies and interstitials.[41] The SRIM software predicts the number of vacancies in the C_{60} layer left by the knocked-out lattice atoms (Fig. S2†). Based on the PL and simulation results, we

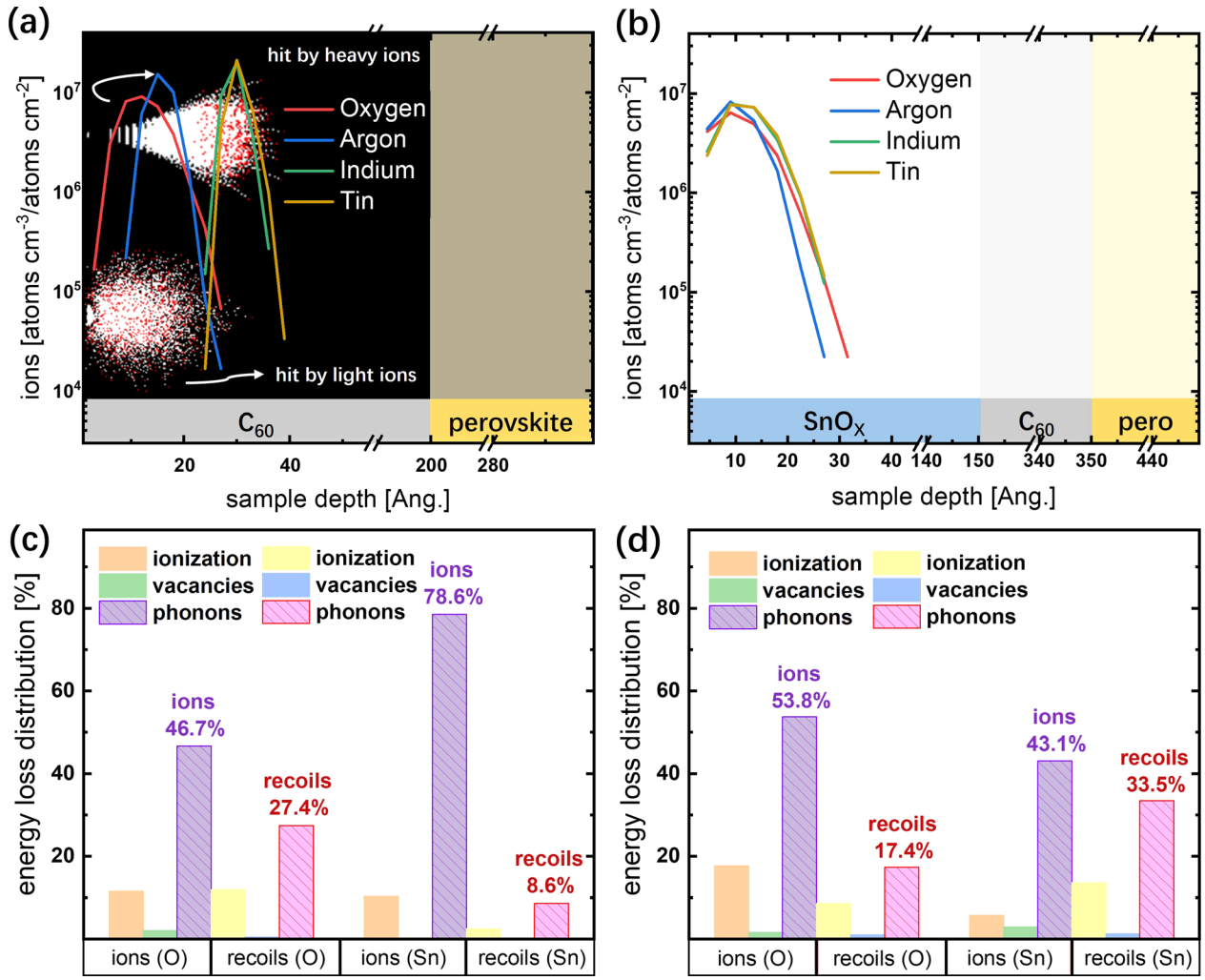

Fig. 6 Penetration depth profile of ions involved in sputtering plasma in (a) the perovskite/C_{60} stack with the distribution of stopped and moving atoms displayed on a black background and (b) the perovskite/C_{60}/SnO_x stack. Energy loss distribution of ions and recoils after oxygen and tin ion bombardment in (c) perovskite/C_{60} stack and (d) perovskite/C_{60}/SnO_x stack.

postulate that a large number of carriers may recombine with the assistance of vacancy defects left by the knocked-out lattice atoms near the C_{60} surface, leading to significant degradation of the PL intensity.

During the TCO sputtering process, the incident ions with high kinetic energies collide with the lattice atoms close to the sample surface, and part of the energy is transferred to the atoms, leading to bond breakage or other structural changes,[19,20] while the remaining energy enables the ions to penetrate deeper into the sample, eventually stopping movement with the remaining energy released as phonons. Fig. 6c shows the energy loss distribution generated from the SRIM simulations. Oxygen ions, the most abundant species in the plasma,[42] generate phonons with 46.7% of their initial kinetic energy of 85 eV, and the recoils contribute an additional 27.4%. Tin ions, the heaviest atoms in the plasma, generated phonons with 78.6% of their initial kinetic energy, and recoils contributed an additional 8.6%. Therefore, the total energy of phonons was 63 eV per incident oxygen ion and 74 eV per incident tin ion within the range of the phonon dispersion relation of C_{60}.[43] It is well known that heat transport in dielectric solids is mainly through the elastic vibration of the lattice, also described as phonon propagation.[44] According to the simulation results, the impinging ions did not penetrate the C_{60} film to reach the perovskite surface; therefore, we speculate that the sputtering damage on the perovskite film is related to phonon propagation. Phonons are quantized lattice vibration modes and are responsible for heat conduction in most non-metallic solids.[45] In the ITO sputtering process, phonons propagate into the perovskite layer in the direction of the film thickness and heat the perovskite surface. However, the energy of phonons reaching the perovskite layer is less than the total energy obtained from ions and atoms due to phonon scattering, including scattering by imperfections,[46] intrinsic-structure scattering combined with internal-boundary scattering,[47] and scattering at solid–solid interfaces.[48] Considering the low energy required to break the chemical bonds in hybrid halide perovskites, such as C–C bonds (3.73 eV), the elevated temperature was perhaps already sufficient to dissociate the bonds at the perovskite surface.[49] Besides, previous reports have revealed that heat can easily degrade the formamidinium cation (FA^+) by breaking the C=N double bonds.[50–52] Investigation of the chemical bonds at the perovskite surface after ITO sputtering is discussed in detail later.

When SnO_x is introduced as a buffer layer, the extra 15 nm thick solid film naturally has a higher potential to protect the underlying perovskite against ion bombardment. To compare the effect of the thickness variations of the stacks, PL spectra were obtained for the glass/ITO/2PACz/perovskite/C_{60} stacks using 35 nm thick C_{60} films, while the conventional thickness of C_{60} was 20 nm. The reduction in PL intensity (Fig. S2†) after ITO sputtering demonstrated that the double layers of C_{60}/SnO_x outperformed the single layer of C_{60} for the same layer thickness. This is mainly because phonons lose a large amount of energy in the SnO_x layer and at the C_{60}/SnO_x interface because of scattering. The ion distribution in the perovskite/C_{60}/SnO_x stack as a function of target depth was also studied, as shown in Fig. 6b. These results demonstrate that all ions had a similar maximum penetration depth of ~3 nm; however, the penetration depth of the heavy ions was less than that in the perovskite/C_{60} stack, which may be associated with the specific mass and atomic radius. The specific mass of SnO_x (6.85 g cm^{-3}) is three times higher than that of the C_{60} (1.65 g cm^{-3}).[53] The fact reflects that the impinging ions collide with more atoms per unit volume and lose energy quicker in the SnO_x film, so the heavy ions have a shorter penetration distance. Because the radius of light ions is much smaller than that of heavy ions, the penetration depth of light ions is less likely to be affected. From the energy loss distribution depicted in Fig. 6d, we conclude that the oxygen ions generated phonons with 53.8% of their initial kinetic energy of 85 eV, and those produced by the recoils accounted for another 17.4%. Tin ions generated phonons with 43.1% of their initial kinetic energy, and recoils produced 33.5%. Therefore, the total energy of the phonons is 61 eV per incident oxygen ion and 72 eV per incident tin ion within the range of the phonon dispersion curve of SnO_x.[54] Both energies are smaller than the total energy of the phonons in the perovskite/C_{60} stack (63 and 74 eV). These results can be explained in terms of E_{disp}, which refers to the minimum kinetic energy required to permanently knock atoms away from the lattice sites. The struck atoms gain energy from a collision, and this energy and the energy of incident ions are released as phonons only if they are lower than the E_{disp} of the lattice.[41] The E_{disp} of Sn is 22 eV, lower than the E_{disp} of C of 25 eV,[55] which means the incident ions and the struck atoms with kinetic energy between 22 and 25 eV could transfer energy to phonons in the C_{60}, but this is not the case in the SnO_x. Therefore, the total energy of phonons in the perovskite/C_{60} stack was slightly higher than that of phonons in the samples with SnO_x layers.

High-resolution X-ray photoelectron spectroscopy (XPS) measurements were used to gain insights into the localized chemical bonding changes on the surface of the perovskite films after ITO sputtering. Fig. 7a compares the Pb 4f core level spectra of three samples: perovskite control (as-prepared), perovskite films with C_{60}, and C_{60}/ITO washed away. The binding energy (BE) of the Pb core level was affected by the elements bonded to it. Specific peaks of Pb $4f_{7/2}$ (~138.6 eV) and Pb $4f_{5/2}$ (~143.4 eV) were present in all samples. The BE of the two Pb 4f peaks of the perovskite with C_{60} washed away (orange curve) overlapped with the peaks of the perovskite control (black curve), indicating that the chemical states of Pb were not affected by washing away C_{60} with CB. A slight shift to a higher BE for both the Pb $4f_{7/2}$ and $4f_{5/2}$ peaks was observed after ITO sputtering (blue curve). This can be attributed to the thermal degradation of the perovskite because the Pb spectra shift toward the direction of mixed halide perovskite decomposition into PbI_2 and $PbBr_2$,[56] which is triggered by the temperature rise at the perovskite surface owing to phonon propagation. Fig. 7b depicts the core level of N 1s, in which two peaks located at the BE of ~400.8 eV and ~402.4 eV representing nitrogen in C=N and C–N bonds confirm the presence of the FA^+ and methylammonium cations (MA^+), respectively.[57] The nitrogen atomic ratio of $FA^+ : MA^+$ in the perovskite control and the perovskite with C_{60} washed away was calculated to be 0.85 : 0.15 (Fig. S3†).

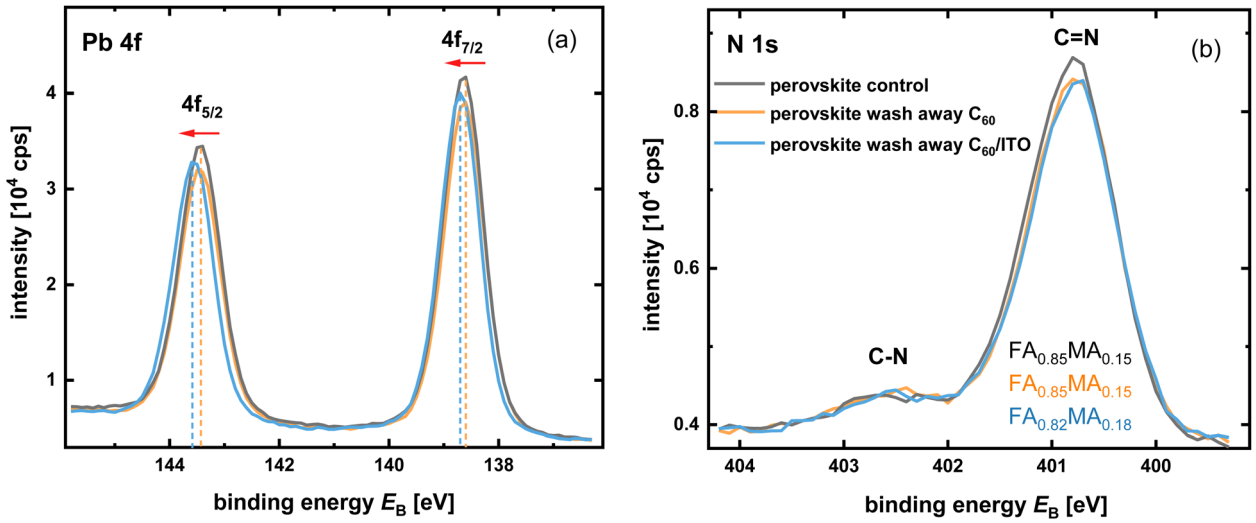

Fig. 7 XPS spectra of (a) Pb 4f and (b) N 1s of three samples.

However, the $FA^+ : MA^+$ ratio decreased to 0.82 : 0.18 after ITO sputtering, suggesting minor loss of FA^+. Meanwhile, the signals of carbon in C–N (~288.5 eV) and C=N (~286.7 eV) bonds found in the C 1s core level spectra also proved the coexistence of FA^+/MA^+,[57] where a shoulder peak to the left of the C=N bonds became apparent with ITO sputtering (Fig. S4†). The deconvoluted C 1s peak of each sample and integrated area under the deconvoluted peaks were fitted using Gaussian functions. The C 1s peak at a BE of ~289.1 eV present in all the samples should be associated with the double-bonded oxidized carbon species O–C=O.[58] The integrated area under the O–C=O bond peaks increased slightly from 613 cps eV to 635 cps eV when the C_{60} layer was washed away. However, after the ITO sputtering, there was a pronounced increase in the integrated area to 967 cps eV. From the SRIM simulation results, we know that oxygen ions cannot penetrate through the C_{60} film and reach the perovskite surface; thus, the dramatic increase in the integrated area under the peak of O–C=O bonds is estimated to be associated with the formation of carbon dangling bonds due to phonon propagation dissociating chemical bonds, which immediately re-bond to the oxygen atoms in the water from ambient air during the transfer of the samples from the glovebox to the XPS spectrometer. The XPS data for the deconvoluted peaks of the C=N bonds in the C 1s core level spectra of the three samples are listed in Table 2 (see ESI†). The ratio of the integrated area under the O=C–O/C=N bond peaks did not change as C_{60} was washed away, suggesting that this approach had a negligible effect. After the ITO sputtering, the ratio increases from 0.37 to 0.48. Analysis of the C=N bonds in the C 1s core level spectra shows that there is an increase in the O=C–O bonds and perhaps a minor loss of FA^+ at the perovskite surface under the effect of ITO sputtering. The peaks observed at a lower BE of ~285.2 eV were attributed to C–C and C–H bonds, which were detected in the contamination of the perovskite surface. The intensities of these peaks increased significantly owing to the removal of C_{60} and C_{60}/ITO with residual impurities. The integrated area under the deconvoluted peaks of the C–N bonds has not been discussed in detail because it is strongly affected by residual impurities, which are difficult to control during transportation. The spectral levels of Cs 3d and I 3d for the three samples almost overlap (Fig. S5†). The core spectral level of Br 3d shifted slightly as C_{60} was washed away; however, no further shift was observed after the ITO sputtering. A shoulder peak at a BE of 530.2 eV in the O1s core level spectra is associated with the ITO residues with C_{60}/ITO washed away,[59] and the strong peaks at ~533.0 eV distinguished in all samples were responsible for the surface absorbed water species. The results demonstrate that a minor loss of FA^+ owing to the dissociation of C=N bonds is the major cause of ion-bombardment-induced sputtering damage to the perovskite film.

To evaluate the impact of the ITO sputtering damage at the device level, we fabricated both opaque and semi-transparent PSCs with distinct device architectures. The opaque devices followed the glass/ITO/SAM/perovskite/C_{60}/SnO_x/Ag structure with a 5 nm thick SnO_x buffer layer. Meanwhile, semi-transparent PSCs were fabricated with a glass/ITO/SAM/perovskite/C_{60}/SnO_x/ITO/Ag structure, employing both 5 nm and 15 nm buffer layers. Fig. 8 shows the *JV* curves derived from the three devices, and the EQE results are presented in the ESI (Fig. S6†). When 5 nm thick SnO_x buffer layers were employed in both devices, the opaque PSC showed an η of 18.8%, but a pronounced S-shaped curve was observed in the semi-transparent PSC, accompanied by a lower η of 11.6%. These results clearly indicate that the S-shape is primarily attributed to sputtering damage rather than variations in band alignment stemming from the addition of the SnO_x buffer layer. The emergence of S-shapes in the *JV* characteristics is commonly attributed to energetic barriers at the contacts[15,20,60,61] for several reasons, such as insulating interfaces,[61] imbalanced charge transport,[62] unfavorable energetic alignment,[63] and Fermi-level pinning by interface states.[64] We adapted the method described in ref. 61 to reveal the origin of the S-shape. A semi-transparent device with a 5 nm-thick SnO_x film, exhibiting

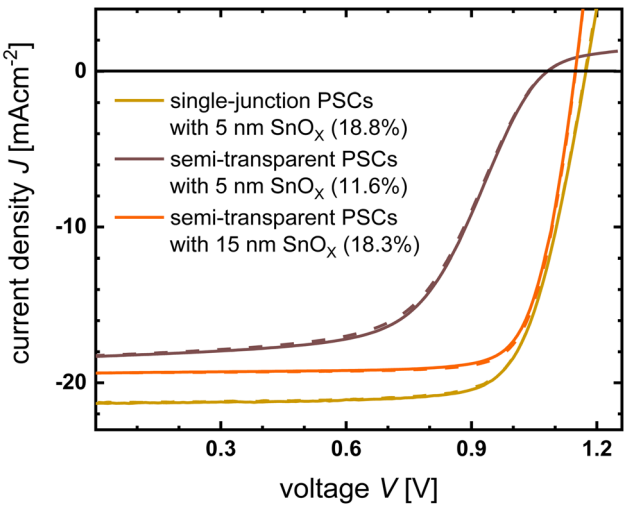

Fig. 8 Current density–voltage (*JV*) curves of single-junction and semi-transparent perovskite solar cells with SnO_x buffer layers. Solid and dashed lines represent the forward and reverse sweeps, respectively.

a pronounced S-shaped *JV* curve, was subjected to illumination across intensities ranging from 0.1 to 1 sun. The obtained *JV* curves were normalized at −0.1 V, where the current was saturated (Fig. S11†). V_{OC} increased as the illumination intensity increased, and the curves crossed near the *X*-axis, suggesting the presence of an extraction barrier for electrons. For comparison, the same method was applied to a semi-transparent device with a 15 nm-thick SnO_x film, revealing a markedly reduced crossing in the non-S-shaped *JV* curves at various light intensities. Therefore, the presence of an extraction barrier at the SnO_x/ITO interface is the reason for the S-shape observed in the *JV* curve of the semi-transparent device with a 5 nm-thick SnO_x film, likely stemming from band alignment issues at the interface. By increasing the SnO_x thickness to 15 nm, the S-shape disappeared, resulting in a significant enhancement of the short-circuit current density (J_{SC}), V_{OC}, and FF of the semi-transparent PSC. This optimization resulted in an optimal η value of 18.3%. This remarkable improvement can be attributed to the effective protection of the perovskite/C_{60} stack from sputtering damage achieved by employing a 15 nm thick SnO_x buffer layer, in contrast to the 5 nm thickness because the energy required a certain thickness to be released after the ion penetration motion stopped.

In conclusion, the ITO sputtering damage to the perovskite/C_{60} stack was attributed to the defects created in the C_{60} layer and the breakage of the C=N bonds at the perovskite surface owing to the heat transfer from the sample surface to the perovskite surface by phonon propagation. The defects and dangling bonds likely act as recombination centers, compromising device performance and long-term stability. The introduction of an SnO_x buffer layer with a critical thickness of 15 nm guarantees the presence of adequate phonon scattering events within the SnO_x layer. Moreover, the C_{60} surface becomes the first solid–solid interface reached by phonons during propagation instead of the perovskite surface, where phonon scattering increases and thermal conduction deteriorates. Consequently, the energy carried by phonons that ultimately reach the perovskite surface is too low to initiate chemical bond dissociation. We have summarized the following suggestions on how to choose a buffer layer for perovskite/silicon tandem solar cells: (1) high transparency can reduce parasitic absorption losses, (2) high specific mass can reduce the penetration depth of impinging ions, (3) low displacement energy can reduce the kinetic energy transferred to phonons, and (4) more internal boundaries can increase the probability of phonon scattering. In cases (3) and (4), a thicker buffer layer can better support the prevention of phonon propagation.

3. Conclusion

In this work, our investigation revealed that the sputtering damage of ITO to perovskite/C_{60} stacks primarily originates from ion bombardment rather than plasma radiation. In contrast, plasma radiation exhibits great potential for suppressing non-radiative recombination within perovskite films. Direct exposure of the perovskite/C_{60} stack to plasma results in the generation of vacancy defects within a few nanometers of the C_{60} surface because of collisions between the impinging ions and lattice atoms. These vacancies likely serve as centers for nonradiative recombination, leading to the deterioration of iV_{OC} and, consequently, a reduction in device efficiency. XPS measurements showed that C=N bonds at the perovskite surface dissociated under plasma irradiation owing to phonon propagation, resulting in a minor loss of FA^+, potentially undermining the device performance. The SnO_x buffer layer mitigated the sputtering damage mainly because of two aspects: (1) less kinetic energy was transferred to phonons owing to better film properties. (2) It is difficult for phonons to propagate to the perovskite surface owing to scattering within the SnO_x layer and C_{60}/SnO_x interface. Overall, we provide insight into the damage mechanism and the consequent working mechanism of the SnO_x buffer layer that shields the perovskite from sputter damage. This work is important for the future optimization of perovskite-based tandem solar cells because further efficiency improvements of such tandem solar cells depend on finding solutions for the compromise between the optical and electrostatic properties of the buffer layer, as well as its ability to block ions during the sputtering process.

Conflicts of interest

There are no conflicts to declare.

Acknowledgements

The authors thank Andreas Schmalen, Johannes Wolff, Daniel Weigand, and Wilfried Reetz for technical assistance. This work was supported by the German Federal Ministry of Economic Affairs and Energy under the framework of the Zeitenwende Project. QY is grateful for financial support from the China Scholarship Council (No. 202004910368) and AK acknowledges Deutscher Akademischer Austauschdienst (DAAD) for the DAAD-PRIME fellowship.

References

1 M. V. Kovalenko, L. Protesescu and M. I. Bodnarchuk, *Science*, 2017, **358**, 745–750.
2 S. De Wolf, J. Holovsky, S. J. Moon, P. Loper, B. Niesen, M. Ledinsky, F. J. Haug, J. H. Yum and C. Ballif, *J. Phys. Chem. Lett.*, 2014, **5**, 1035–1039.
3 L. Krückemeier, B. Krogmeier, Z. Liu, U. Rau and T. Kirchartz, *Adv. Energy Mater.*, 2021, **11**, 2003489.
4 N.-G. Park and K. Zhu, *Nat. Rev. Mater.*, 2020, **5**, 333–350.
5 Z. Li, T. R. Klein, D. H. Kim, M. Yang, J. J. Berry, M. F. A. M. van Hest and K. Zhu, *Nat. Rev. Mater.*, 2018, **3**, 1–20.
6 M. A. Green, A. Ho-Baillie and H. J. Snaith, *Nat. Photonics*, 2014, **8**, 506–514.
7 J. Y. Kim, J. W. Lee, H. S. Jung, H. Shin and N. G. Park, *Chem. Rev.*, 2020, **120**, 7867–7918.
8 N. J. Jeon, J. H. Noh, Y. C. Kim, W. S. Yang, S. Ryu and S. I. Seok, *Nat. Mater.*, 2014, **13**, 897–903.
9 J. Park, J. Kim, H. S. Yun, M. J. Paik, E. Noh, H. J. Mun, M. G. Kim, T. J. Shin and S. I. Seok, *Nature*, 2023, **616**, 724–730.
10 N. M. Haegel, P. Verlinden, M. Victoria, P. Altermatt, H. Atwater, T. Barnes, C. Breyer, C. Case, S. D. Wolf, C. Deline, M. Dharmrin, B. Dimmler, M. Gloeckler, J. C. Goldschmidt, B. Hallam, S. Haussener, B. Holder, U. Jaeger, A. J. Waldau, I. Kaizuka, H. Kikusato, B. Kroposki, S. Kurtz, K. Matsubara, S. Nowak, K. Ogimoto, C. Peter, I. M. Peters, S. Philipps, M. Powalla, U. Rau, T. Reindl, M. Roumpani, K. Sakurai, C. n. Schorn, P. Schossig, R. Schlatmann, R. Sinton, A. Slaoui, B. L. Smith, P. Schneidewind, B. Stanbery, M. Topic, W. Tumas, J. Vasi, M. Vetter, E. Weber, A. W. Weeber, A. Weidlich, D. Weiss and A. W. Bett, *Science*, 2023, **380**, 39–42.
11 Z. Zhu, K. Mao and J. Xu, *J. Energy Chem.*, 2021, **58**, 219–232.
12 M. Jošt, L. Kegelmann, L. Korte and S. Albrecht, *Adv. Energy Mater.*, 2020, **10**, 1904102.
13 J. P. Mailoa, C. D. Bailie, E. C. Johlin, E. T. Hoke, A. J. Akey, W. H. Nguyen, M. D. McGehee and T. Buonassisi, *Appl. Phys. Lett.*, 2015, **106**, 121105.
14 *NREL Transforming ENERGY*, **https://www.nrel.gov/pv/cell-efficiency.html**, accessed: February 2024.
15 J. Werner, G. Dubuis, A. Walter, P. Löper, S.-J. Moon, S. Nicolay, M. Morales-Masis, S. De Wolf, B. Niesen and C. Ballif, *Sol. Energy Mater. Sol. Cells*, 2015, **141**, 407–413.
16 E. Aydin, M. De Bastiani, X. Yang, M. Sajjad, F. Aljamaan, Y. Smirnov, M. N. Hedhili, W. Liu, T. G. Allen, L. Xu, E. Van Kerschaver, M. Morales-Masis, U. Schwingenschlögl and S. De Wolf, *Adv. Funct. Mater.*, 2019, **29**, 1901741.
17 K. Ellmer and T. Welzel, *J. Mater. Res.*, 2012, **27**, 765–779.
18 P. F. Carcia, R. S. McLean, M. H. Reilly, Z. G. Li, L. J. Pillione and R. F. Messier, *J. Vac. Sci. Technol., A*, 2003, **21**, 745–751.
19 Q. H. Fan, M. Deng, X. Liao and X. Deng, *J. Appl. Phys.*, 2009, **105**, 033304.
20 H. Kanda, A. Uzum, A. K. Baranwal, T. A. N. Peiris, T. Umeyama, H. Imahori, H. Segawa, T. Miyasaka and S. Ito, *J. Phys. Chem. C*, 2016, **120**, 28441–28447.
21 K. P. S. Zanoni, A. Paliwal, M. A. Hernández-Fenollosa, P. A. Repecaud, M. Morales-Masis and H. J. Bolink, *Adv. Mater. Technol.*, 2022, **7**, 2101747.
22 S. Mariotti, K. Jäger, M. Diederich, M. S. Härtel, B. Li, K. Sveinbjörnsson, S. Kajari-Schröder, R. Peibst, S. Albrecht, L. Korte and T. Wietler, *Sol. RRL*, 2022, **6**, 2101066.
23 E. Aydin, C. Altinkaya, Y. Smirnov, M. A. Yaqin, K. P. S. Zanoni, A. Paliwal, Y. Firdaus, T. G. Allen, T. D. Anthopoulos, H. J. Bolink, M. Morales-Masis and S. De Wolf, *Matter*, 2021, **4**, 3549–3584.
24 Z. Ma, Y. Dong, R. Wang, Z. Xu, M. Li and Z. Tan, *Adv. Mater.*, 2023, **35**, e2307502.
25 M. Härtel, B. Li, S. Mariotti, P. Wagner, F. Ruske, S. Albrecht and B. Szyszka, *Sol. Energy Mater. Sol. Cells*, 2023, **252**, 112180.
26 D. Hamaguchi, S.-i. Kobayashi, T. Uchida, Y. Sawada, H. Lei and Y. Hoshi, *Jpn. J. Appl. Phys.*, 2016, **55**, 106501.
27 Y. Smirnov, L. Schmengler, R. Kuik, P. A. Repecaud, M. Najafi, D. Zhang, M. Theelen, E. Aydin, S. Veenstra, S. De Wolf and M. Morales-Masis, *Adv. Mater. Technol.*, 2021, **6**, 2000856.
28 S. Zhu, X. Yao, Q. Ren, C. Zheng, S. Li, Y. Tong, B. Shi, S. Guo, L. Fan and H. Ren, *Nano Energy*, 2018, **45**, 280–286.
29 Y. Kuang, B. Macco, B. Karasulu, C. K. Ande, P. C. P. Bronsveld, M. A. Verheijen, Y. Wu, W. M. M. Kessels and R. E. I. Schropp, *Sol. Energy Mater. Sol. Cells*, 2017, **163**, 43–50.
30 T. W. Jones, A. Osherov, M. Alsari, M. Sponseller, B. C. Duck, Y.-K. Jung, C. Settens, F. Niroui, R. Brenes, C. V. Stan, Y. Li, M. Abdi-Jalebi, N. Tamura, J. E. Macdonald, M. Burghammer, R. H. Friend, V. Bulović, A. Walsh, G. J. Wilson, S. Lilliu and S. D. Stranks, *Energy Environ. Sci.*, 2019, **12**, 596–606.
31 J. T.-W. Wang, Z. Wang, S. Pathak, W. Zhang, D. W. deQuilettes, F. Wisnivesky-Rocca-Rivarola, J. Huang, P. K. Nayak, J. B. Patel, H. A. Mohd Yusof, Y. Vaynzof, R. Zhu, I. Ramirez, J. Zhang, C. Ducati, C. Grovenor, M. B. Johnston, D. S. Ginger, R. J. Nicholas and H. J. Snaith, *Energy Environ. Sci.*, 2016, **9**, 2892–2901.
32 G. Kim, H. Min, K. S. Lee, D. Y. Lee, S. M. Yoon and S. I. Seok, *Science*, 2020, **370**, 108–112.
33 M. Saliba, T. Matsui, J. Y. Seo, K. Domanski, J. P. Correa-Baena, M. K. Nazeeruddin, S. M. Zakeeruddin, W. Tress, A. Abate, A. Hagfeldt and M. Gratzel, *Energy Environ. Sci.*, 2016, **9**, 1989–1997.
34 J. Zhao, Y. Deng, H. Wei, X. Zheng, Z. Yu, Y. Shao, J. H. Jeffrey and E. Shield, *Sci. Adv.*, 2017, **3**, eaao5616.
35 G. Williamson and W. Hall, *Acta Metall.*, 1953, **1**, 22–31.
36 G. Su, R. Yu, Y. Dong, Z. He, Y. Zhang, R. Wang, Q. Dang, S. Sha, Q. Lv, Z. Xu, Z. Liu, M. Li and Z. a. Tan, *Adv. Energy Mater.*, 2023, **14**, 2303344.
37 H. Tsai, R. Asadpour, J.-C. Blancon, C. C. Stoumpos, O. Durand, J. W. Strzalka, B. Chen, R. Verduzco,

P. M. Ajayan, S. Tretiak, J. Even, M. A. Alam, M. G. Kanatzidis, W. Nie and A. D. Mohite, *Science*, 2018, **360**, 67–70.
38 O. Carp, *Prog. Solid State Chem.*, 2004, **32**, 33–177.
39 M. A. Boda, C. Chen, X. He, L. Wang and Z. Yi, *J. Am. Ceram. Soc.*, 2023, **106**, 3584–3593.
40 T. C. Wei, H. P. Wang, T. Y. Li, C. H. Lin, Y. H. Hsieh, Y. H. Chu and J. H. He, *Adv. Mater.*, 2017, **29**, 1701789.
41 J. F. Ziegler, M. D. Ziegler and J. P. Biersack, *SRIM–The Stopping and Range of Ions in Matter (2010)*, 2010.
42 T. Welzel and K. Ellmer, *Vak. Forsch. Prax.*, 2013, **25**, 52–56.
43 J. Yu, R. K. Kalia and P. Vashishta, *Appl. Phys. Lett.*, 1993, **63**, 3152–3154.
44 P. G. Klemens, *Proc. R. Soc. London, Ser. A*, 1951, **208**, 108–133.
45 Y. K. Koh, in *Encyclopedia of Nanotechnology*, Springer, Dordrecht, 2012, pp. 2704–2711, DOI: **10.1007/978-90-481-9751-4**.
46 J. M. Ziman, *Electrons and Phonons: The Theory of Transport Phenomena in Solids*, Oxford University Press, 2001.
47 G. K. Chang and R. E. Jones, *Phys. Rev.*, 1962, **126**, 2055–2058.
48 D. G. Cahill, *Microscale Thermophys. Eng.*, 1997, **1**, 85–109.
49 H.-K. Kim, D.-G. Kim, K.-S. Lee, M.-S. Huh, S. H. Jeong and K. I. Kim, *Appl. Phys. Lett.*, 2005, **86**, 183503.
50 E. J. Juarez-Perez, L. K. Ono and Y. Qi, *J. Mater. Chem. A*, 2019, **7**, 16912–16919.
51 F. C. Schaefer, I. Hechenbleikner, G. A. Peters and V. Wystrach, *Chem. Soc.*, 1959, **81**, 1466–1470.
52 W. T. M. Van Gompel, R. Herckens, G. Reekmans, B. Ruttens, J. D'Haen, P. Adriaensens, L. Lutsen and D. Vanderzande, *J. Phys. Chem. C*, 2018, **122**, 4117–4124.
53 F. Lang, M. Jost, K. Frohna, E. Kohnen, A. Al-Ashouri, A. R. Bowman, T. Bertram, A. B. Morales-Vilches, D. Koushik, E. M. Tennyson, K. Galkowski, G. Landi, M. Creatore, B. Stannowski, C. A. Kaufmann, J. Bundesmann, J. Rappich, B. Rech, A. Denker, S. Albrecht, H. C. Neitzert, N. H. Nickel and S. D. Stranks, *Joule*, 2020, **4**, 1054–1069.
54 K. Parlinski and Y. Kawazoe, *Eur. Phys. J. B*, 2000, **13**, 679–683.
55 M. Nastasi, J. Mayer and J. K. Hirvonen, *Ion-Solid Interactions – Fundamentals and Applications*, Cambridge University Press, 1996.
56 I. S. Zhidkov, D. W. Boukhvalov, A. F. Akbulatov, L. A. Frolova, L. D. Finkelstein, A. I. Kukharenko, S. O. Cholakh, C.-C. Chueh, P. A. Troshin and E. Z. Kurmaev, *Nano Energy*, 2021, **79**, 105421.
57 T. J. Jacobsson, J. P. Correa-Baena, E. Halvani Anaraki, B. Philippe, S. D. Stranks, M. E. Bouduban, W. Tress, K. Schenk, J. Teuscher, J. E. Moser, H. Rensmo and A. Hagfeldt, *J. Am. Chem. Soc.*, 2016, **138**, 10331–10343.
58 J. C. Vickerman and I. S. Gilmore, *Surface Analysis – The Principal Techniques*, John Wiley & Sons, 2009.
59 J. S. Kim, P. K. H. Ho, D. S. Thomas, R. H. Friend, F. Cacialli, G.-W. Bao and S. F. Y. Li, *Chem. Phys. Lett.*, 1999, **315**, 307–312.
60 O. J. Sandberg, J. Kurpiers, M. Stolterfoht, D. Neher, P. Meredith, S. Shoaee and A. Armin, *Adv. Mater. Interfaces*, 2020, **7**, 2000041.
61 W. Tress and O. Inganäs, *Sol. Energy Mater. Sol. Cells*, 2013, **117**, 599–603.
62 W. Tress, A. Petrich, M. Hummert, M. Hein, K. Leo and M. Riede, *Appl. Phys. Lett.*, 2011, **98**, 063301.
63 J. Wagner, M. Gruber, A. Wilke, Y. Tanaka, K. Topczak, A. Steindamm, U. Hörmann, A. Opitz, Y. Nakayama, H. Ishii, J. Pflaum, N. Koch and W. Brütting, *J. Appl. Phys.*, 2012, **111**, 054509.
64 A. M. Cowley and S. M. Sze, *J. Appl. Phys.*, 1965, **36**, 3212–3220.